PHYSICAL REVIEW FLUIDS **3**, 014612 (2018)

Evolution of passive scalar statistics in a spatially developing turbulence

I. Paul,[*] G. Papadakis, and J. C. Vassilicos
Department of Aeronautics, Imperial College London, London SW7 2AZ, United Kingdom

(Received 24 October 2017; published 31 January 2018)

We investigate the evolution of passive scalar statistics in a spatially developing turbulence using direct numerical simulation. Turbulence is generated by a square grid element, which is heated continuously, and the passive scalar is temperature. The square element is the fundamental building block for both regular and fractal grids. We trace the dominant mechanisms responsible for the dynamical evolution of scalar-variance and its dissipation along the bar and grid-element centerlines. The scalar-variance is generated predominantly by the action of the mean scalar gradient behind the bar and is transported laterally by turbulent fluctuations to the grid-element centerline. The scalar-variance dissipation (proportional to the scalar-gradient variance) is produced primarily by the compression of the fluctuating scalar-gradient vector by the turbulent strain rate, while the contribution of mean velocity and scalar fields is negligible. Close to the grid element the scalar spectrum exhibits a well-defined $-5/3$ power-law, even though the basic premises of the Kolmogorov-Obukhov-Corrsin theory are not satisfied (the fluctuating scalar field is highly intermittent, inhomogeneous, and anisotropic, and the local Corrsin-microscale-Péclet number is small). At this location, the PDF of scalar gradient production is only slightly skewed towards positive, and the fluctuating scalar-gradient vector aligns only with the compressive strain-rate eigenvector. The scalar-gradient vector is stretched or compressed stronger than the vorticity vector by turbulent strain rate throughout the grid-element centerline. However, the alignment of the former changes much earlier in space than that of the latter, resulting in scalar-variance dissipation to decay earlier along the grid-element centerline compared to the turbulent kinetic energy dissipation. The universal alignment behavior of the scalar-gradient vector is found far downstream, although the local Reynolds and Péclet numbers (based on the Taylor and Corrsin length scales, respectively) are low.

DOI: 10.1103/PhysRevFluids.3.014612

I. INTRODUCTION

A passive scalar is transported by the flow but does not react back, i.e., it does not influence the carrier flow. Examples include small variations of temperature and pollutant concentration. Understanding the statistical behavior of scalar fluctuations and their gradients is important from both the application as well as the fundamental points of view. Most of the industrial processes (for instance, heat exchange, mixing, combustion) involve the transport of scalar by a turbulent flow. Similarly, understanding of micromixing, and thus arriving at an effective mixing model, requires knowledge of the fluctuating scalar gradients [1]. The study of passive scalar is also fundamental to the understanding of turbulence itself. Numerous studies on various aspects of scalar turbulence have appeared in the literature and are reviewed in Refs. [2–9].

The dynamics of passive scalar turbulence have been explored theoretically [10,11], experimentally [1,12–15], and numerically [16–21] for various flow configurations. Some flows have shear (jets or wakes), and some are shear-free (grid turbulence). In most shear-free flows, a mean scalar

---

[*] p.immanuvel@imperial.ac.uk

gradient is imposed at the inlet [22–26], but there are also studies where the grid is heated [12,27,28]. It is important to stress that almost all of the previous studies of shear-free scalar turbulence are either experiments carried out rather far downstream of the grid, or periodic box direct numerical simulations with an imposed mean scalar gradient. Thus, they have analyzed mostly the scalar properties in turbulence, which is designed to be close to homogeneous isotropic turbulence (HIT).

The last decade has witnessed an interest in turbulent flows generated by fractal grids. Since the work of Seoud and Vassilicos [29], many studies have focused on the turbulent flow generated by multiscale or fractal grids [30–32]. Recently, Valente and Vassilicos [33], Zhou *et al.* [34–36], and Paul *et al.* [37] have shown that the turbulence generated by a single square grid element shares similarities with that generated by a fractal square grid. In both flows, there is an extended turbulent production region followed by a decay region. The production region is characterized by increasing turbulent intensity, which decays farther downstream. Previous experimental and numerical studies of Refs. [37–40] have shown that the dynamics of velocity gradients in the near-grid region are different from the HIT case. In particular, the velocity spectrum has a $-5/3$ power-law slope even in the near-grid region where the turbulence is highly inhomogeneous and developing. In that region, the Q-R diagrams (where Q and R are the second and third invariants of the velocity gradient tensor) are not developed, and strain dominates enstrophy.

Previous works have demonstrated significantly increased turbulent scalar fluxes in the cross-stream direction in the lee of a fractal grid, and proposed a mechanism to explain this behavior [41–45]. To the best of authors' knowledge, there are no comprehensive studies on the dynamical evolution of scalar-variance and scalar gradients in turbulence generated by fractal or single square grids.

The central aim of this paper is not only to study the statistical behavior of scalar gradients, but also to investigate their relationship with velocity gradients. The turbulence is generated by a single square grid element which is heated continuously, and the passive scalar is temperature. The present work complements the previous study of the authors on the evolution of velocity gradients in a turbulent flow generated by the same geometry [37]. The scalar gradient analysis aims to answer the following five questions:

(1) How are the large- and small-scale terms of scalar turbulence generated and transported in this spatially developing turbulence? We identify the dominant mechanisms responsible for the transport of these quantities in Sec. III.

(2) It is sometimes believed that the evolution of scalar dissipation is similar to that of the mean enstrophy of fluctuations [46]. Do these quantities indeed behave similarly in the examined flow? We report on the similarities and differences along the grid-element and bar centerlines in Secs. III B and VI. In Sec. V we explain the observed trends by probing more deeply into the production of these quantities due to turbulent stretching and compressing by the strain rate.

(3) Does the $-5/3$ power-law slope of the scalar spectrum appear in the inhomogeneous, near grid-element region? Previous studies have established that for HIT the $-5/3$ slope appears over a wider range of frequencies than the velocity spectrum (refer to the review in Ref. [6]). It is not clear if this is also true when the scalar field is highly inhomogeneous and developing. We explore this question in Sec. IV.

(4) If indeed there is a power-law in the scalar spectrum in the near grid element region, how do the small-scale scalar dynamics correlate with the scalar cascade? The stretching of the vorticity vector is believed to be closely associated with the energy cascade in turbulent flows. The equivalent process in the scalar cascade is the stretching and compressing of the passive scalar-gradient vector. In Sec. V we correlate the behavior of scalar small-scale terms with the $-5/3$ power-law slope of the scalar spectra.

(5) How do the scalar spectrum and the scalar gradient dynamics evolve from the near grid-element region to the far downstream? Since the turbulence is developing, the dynamics of scalar gradients are also expected to vary, and we study this evolution throughout this paper.

The rest of the paper is organized as follows. The next section provides the details of the numerical setup. The budgets of large- and small-scale quantities (scalar-variance and dissipation, respectively)

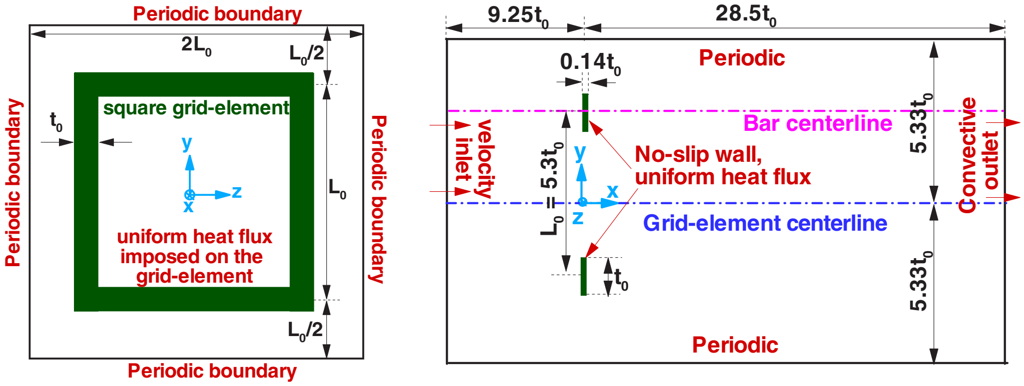

(a) (b)

FIG. 1. Sketch of the computational domain: (a) front view, (b) side view at plane $z/t_0 = 0$ (sketches not to scale).

are discussed in Sec. III. Then we analyze the scalar spectra in Sec. IV and the relation with small-scale stretching and compressing (Sec. V). The evolution of scalar-variance and turbulent kinetic energy dissipation rates are analyzed in Sec. VI. Finally, we summarize the main conclusions in Sec. VII.

II. NUMERICAL METHOD AND COMPUTATIONAL PARAMETERS

Throughout the paper, the instantaneous, mean, and fluctuating velocity fields are denoted as u_i^*, U_i, and u_i respectively (where $i = 1,2,3$). The corresponding variables for pressure and temperature are p^*, P, p, and T^*, $\langle T^* \rangle$, T. Throughout the paper, the brackets $\langle\,\rangle$ are used to represent the time-averaging operation. The continuity, momentum, and scalar conservation equations are written as

$$\frac{\partial u_i^*}{\partial x_i} = 0, \tag{1}$$

$$\frac{\partial u_i^*}{\partial t} + u_j^* \frac{\partial u_i^*}{\partial x_j} = -\frac{1}{\rho}\frac{\partial p^*}{\partial x_i} + \nu \frac{\partial^2 u_i^*}{\partial x_j \partial x_j}, \tag{2}$$

$$\frac{\partial T^*}{\partial t} + u_j^* \frac{\partial T^*}{\partial x_j} = \alpha \frac{\partial^2 T^*}{\partial x_j \partial x_j}, \tag{3}$$

where ρ,ν,α are the density, kinematic viscosity, and thermal diffusivity of the fluid, respectively.

These equations are solved using the in-house parallel solver, Pantarhei. The solver is based on unstructured finite volume discretization in a collocated variable arrangement. The convective and diffusive spatial terms are discretized using the second-order central-differencing scheme, while the second-order backward scheme is employed for time advancement. The code is parallelized using the PETSc libraries [47]. More details about the solver can be found in Refs. [37,48–50].

The front view of the computational domain in the y-z plane is depicted in Fig. 1(a). The origin of the coordinate system is located at the center of the element. The bar has lateral thickness $t_0 = 43$ mm, length $L_0 = 229$ mm, and streamwise thickness 6 mm. The blockage ratio is 20%. A characteristic wake interaction length scale, defined as $x^* = L_0^2/t_0$ (refer to Ref. [30]), is used to normalize the streamwise distance downstream of the grid element. A side view of the computational domain at plane $z/t_0 = 0$, with details on the size of the domain and type of boundaries, is shown in Fig. 1(b) .

Uniform velocity and temperature profiles are prescribed at the inlet (U_∞ and T_∞, respectively), and a convective boundary condition is imposed at the outlet. All lateral boundaries are periodic. On

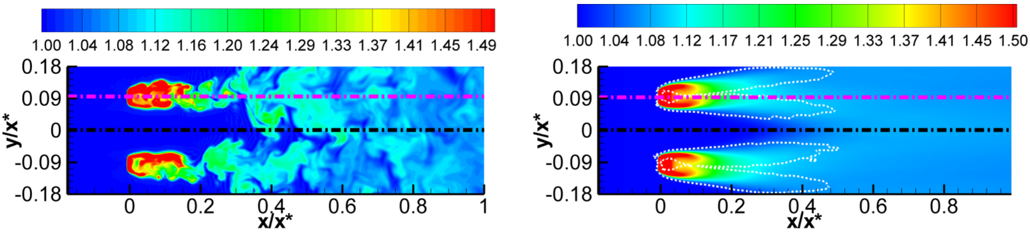

(a) (b)

FIG. 2. Contours of (a) instantaneous temperature and (b) mean temperature fields. The isocontours range from 1 to 1.5 T_∞. The white dotted line in (b) is the isoline of normalized mean vorticity vector magnitude ($\langle|\boldsymbol{\omega}^*|\rangle t_0/U_\infty$) of 0.18. The black dotted-dashed line is the centerline of the grid element, and the bar centerline is represented by a pink dotted-dashed line.

the grid-element surface, a no-slip condition is applied for velocity and uniform heat flux ($\dot{q}_w$) for temperature. The Reynolds number based on the the free-stream velocity U_∞ and the bar length L_0 is $\mathrm{Re}_{L_0} = 2650$, while based on the lateral thickness t_0 is $\mathrm{Re}_{t_0} = 500$. The Prandtl number, $\mathrm{Pr} = \nu/\alpha$, is 0.71.

The same mesh employed in our previous study [37] is also used for this paper. It was shown in Ref. [37] that the ratio of a characteristic mesh size to the Kolmogorov length scale is less than 1 throughout the computational domain. Since $\mathrm{Pr} < 1$, the Obukhov-Corrsin scale $\eta_{\mathrm{OC}}[\eta_{\mathrm{OC}} = \eta \mathrm{Pr}^{-3/4}$ where $\eta = (\nu^3/\epsilon_k)^{1/4}$ is the Kolmogorov length scale and $\epsilon_k = 2\nu\langle s_{ij}s_{ij}\rangle$ where $s_{ij} = \frac{1}{2}(\frac{\partial u_i}{\partial x_j} + \frac{\partial u_j}{\partial x_i})$ is the turbulent strain rate] is larger than the Kolmogorov length scale. Therefore, the mesh resolution is finer for the scalar field compared to the velocity field. At worst, the mesh resolution is $0.63\eta_{\mathrm{OC}}$ in the whole domain. More details about the mesh and the numerical setup are presented in Ref. [37].

The validation of the solver against experiments for one-point velocity and velocity-gradient statistics is presented in Ref. [37]. We rely upon this validation for the present study since there are no experiments available for the scalar field.

III. BALANCE OF TRANSPORT EQUATIONS

In this section we investigate the dynamics and transport mechanisms of large and small scales of scalar turbulence. The large-scale terms are characterized by fluctuations and the small-scale terms by fluctuation gradients [51]. scalar-variance is considered a large-scale term while scalar-gradient variance is a small-scale term. The transport equations of these quantities are studied along the bar and grid-element centerlines because of the different dynamics prevalent at these two locations.

The scalar field under consideration is visualized first. Contours of the instantaneous scalar field are depicted in Fig. 2(a). The scalar is being injected into the wake by heating the grid element. Vorticity is produced at the walls and shed into the wake. Both scalar and vorticity have therefore initially the same length scale. For the time instant shown in the figure, the scalar wakes behind the bars start meeting at $x/x^* \approx 0.4$. As shown later, the scalar wakes meet at $x/x^* \approx 0.2$ on average, which is similar to the location reported in Ref. [37] for the meeting of vortical wakes.

The time-averaged scalar field is shown in Fig. 2(b). The isoline of normalized mean vorticity vector magnitude is superimposed in order to compare the spreading rate of vorticity and scalar wakes. The two rates are similar, as expected [52]. A mean recirculation region forms behind the bars, and its length is approximately $3.7t_0$ (or $0.13x^*$). The scalar is trapped inside this region, leading to high values in the centerline [depicted as a small circular red area behind the bars in Fig. 2(b)].

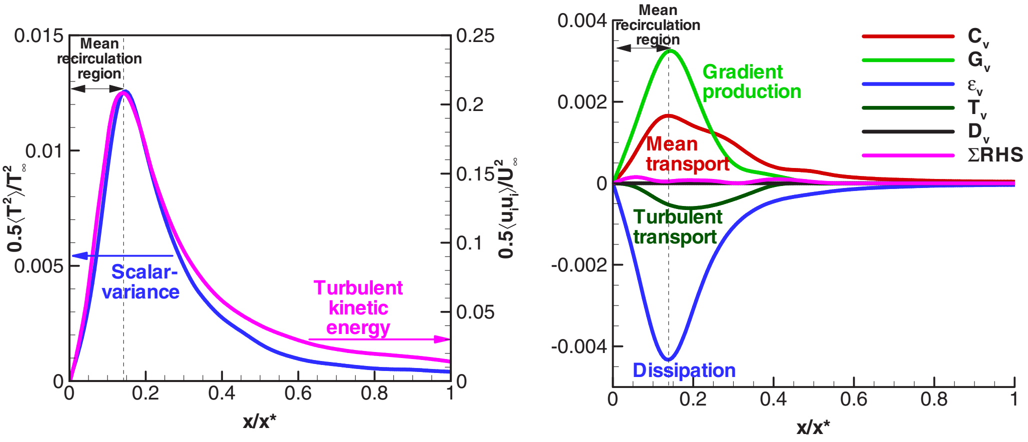

(a)

(b)

FIG. 3. (a) Evolution of scalar-variance and turbulent kinetic energy along the bar centerline; (b) evolution of budget terms of scalar-variance along the bar centerline. All terms are normalized by $U_\infty T_\infty^2/t_0$.

A. Scalar-variance balance

The transport equation of scalar-variance $\frac{1}{2}\langle T^2\rangle$ can be written as (refer to Ref. [52])

$$\frac{\partial\left(\left\langle\frac{1}{2}T^2\right\rangle\right)}{\partial t} = \underbrace{-U_j\frac{\partial\left(\left\langle\frac{1}{2}T^2\right\rangle\right)}{\partial x_j}}_{C_v} \underbrace{-\langle u_j T\rangle\frac{\partial\langle T^*\rangle}{\partial x_j}}_{G_v} \underbrace{-\alpha\left\langle\frac{\partial T}{\partial x_j}\frac{\partial T}{\partial x_j}\right\rangle}_{\epsilon_v} \underbrace{-\frac{\partial}{\partial x_j}\left\langle\frac{1}{2}u_j T^2\right\rangle}_{T_v} \underbrace{+\alpha\frac{\partial}{\partial x_j}\left(\frac{\partial\frac{1}{2}\langle T^2\rangle}{\partial x_j}\right)}_{D_v}, \quad (4)$$

where C_v is the mean flow convection, G_v is the production by mean scalar gradient, ϵ_v is the scalar dissipation, T_v is the transport by turbulent fluctuations, and D_v is the molecular diffusion. The transient term in the left-hand side is 0, as only time-averaged quantities are considered. Note that ϵ_v is proportional to the scalar-gradient variance $\langle\frac{\partial T}{\partial x_j}\frac{\partial T}{\partial x_j}\rangle$, the proportionality constant being the thermal diffusivity, α.

Figure 3(a) presents the evolutions of scalar-variance and turbulent kinetic energy along the bar centerline. The scalar-variance increases from $x = 0$ till the end of the mean recirculation region (i.e., $x = 0.13x^*$) and then decays downstream. This trend is very similar to the evolution of the turbulent kinetic energy, but the scalar-variance decays slightly faster. The dynamics of scalar-variance is further analyzed through the evolution of the budget terms [Fig. 3(b)]. Close to the bar, the mean scalar gradients generate scalar-variance, which is transported by the mean flow. The production and transport terms increase until the end of the mean recirculation region, while they are balanced by the turbulent transport and dissipation terms. Downstream of the mean recirculation region, the gradient production and mean transport decrease. After $x/x^* \approx 0.5$, the turbulent transport term becomes negligible, and the scalar-variance decays due to dissipation while it is carried by the mean flow.

We now turn our attention to the evolution of scalar-variance and turbulent kinetic energy along the grid-element centerline [Fig. 4(a)]. Although the variation of these quantities was very similar behind the bars as demonstrated in Fig. 3(a), they exhibit intriguing differences along the grid-element centerline. First, the scalar-variance is negligible for $x/x^* < 0.2$, but the kinetic energy is clearly not. The latter is generated by the work done by pressure [37], a mechanism which is absent for the scalar-variance. More specifically, the presence of vortex shedding behind the bars generates a fluctuating pressure field that correlates with the velocity in the grid-element centerline, making the generation term $-\frac{\partial(u_j p)}{\partial x_j}$ for kinetic energy dominant in the lee of the grid. Second, the onset of scalar-variance decay occurs upstream compared to that of the turbulent kinetic energy. While

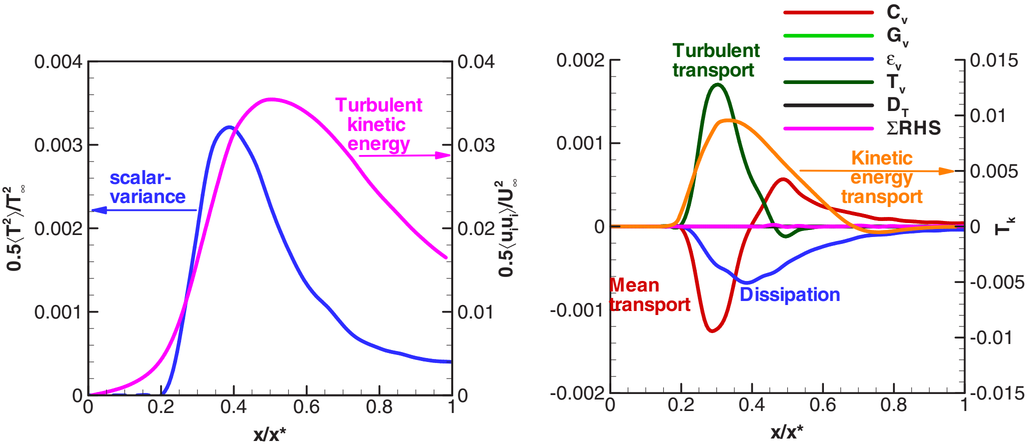

(a)

(b)

FIG. 4. (a) Evolution of scalar-variance and turbulent kinetic energy along the grid-element centerline; (b) evolution of budget terms of scalar-variance along the grid-element centerline. All terms are normalized by $U_\infty T^2_\infty/t_0$. The transport due to fluctuations of the turbulent kinetic energy is also shown.

the turbulent kinetic energy starts decaying around $x/x^* \approx 0.5$, the decay of scalar-variance starts around 0.4. Comparing Figs. 3(a) and 4(a), it is interesting that the variations of scalar-variance and turbulent kinetic energy are qualitatively similar, with both quantities reaching a peak value at exactly the same location along the bar centerline, but along the grid-element centerline, their behavior is markedly different. They peak at different locations, and the decay rate of scalar-variance is significantly faster compared to that of the turbulent kinetic energy.

The budget terms, shown in Fig. 4(b), provide insight into the evolution of scalar-variance along the grid-element centerline. The first term that becomes active is the turbulent transport term, $T_v = -\frac{\partial}{\partial x_j}\langle\frac{1}{2}u_j T^2\rangle$. The two lateral directions ($j = 2{,}3$) make the largest contribution to this term, indicating that the scalar-variance, which was produced by the mean scalar gradients near the bar, is brought to the grid-element centerline through the lateral motion of the bar wakes. The average meeting point of the thermal wakes is $x/x^* \approx 0.2$, and this marks the location of rapid growth of turbulent transport (and consequently scalar-variance). The turbulent transport term is balanced by the mean convection and dissipation. Turbulent transport becomes negligible around $x/x^* \approx 0.5$. Farther downstream, the scalar-variance is carried by the mean flow while it is dissipated.

The differences in the decay rate of turbulence kinetic energy and dissipation have been studied before, but mainly for homogeneous isotropic turbulence [12,53,54]. Theoretical analysis shows that, if the spectra of kinetic energy and scalar peak at wave numbers that are of the same order, the exponents of the decay equation are similar (values 1.38 and 1.48 are reported in Ref. [54]). If, however, the scalar is injected at a much larger wave number, then the instantaneous decay rate of scalar-variance is much larger compared to the aforementioned values. Such a behavior was observed in Ref. [12] on heated grid experiments, and a theoretical explanation was proposed in Ref. [54]. The (initially small) temperature integral scale grows to approach the velocity integral scale, and during this time larger decay rates are predicted. It is unlikely that this explanation is valid also for our case. First, the anomalous behavior was measured when the scalar was introduced by placing a heated parallel array of fine wires (a mandolin) downstream of the unheated grid. This results in the scalar and velocity spectra to have different spectral peaks, but in our case vorticity and scalar are both injected at the grid location. Second, the measurements of Ref. [12] were carried out far from the grid (at location 80 times the grid size, as mentioned in their Fig. 15), while our analysis focuses very close to the grid.

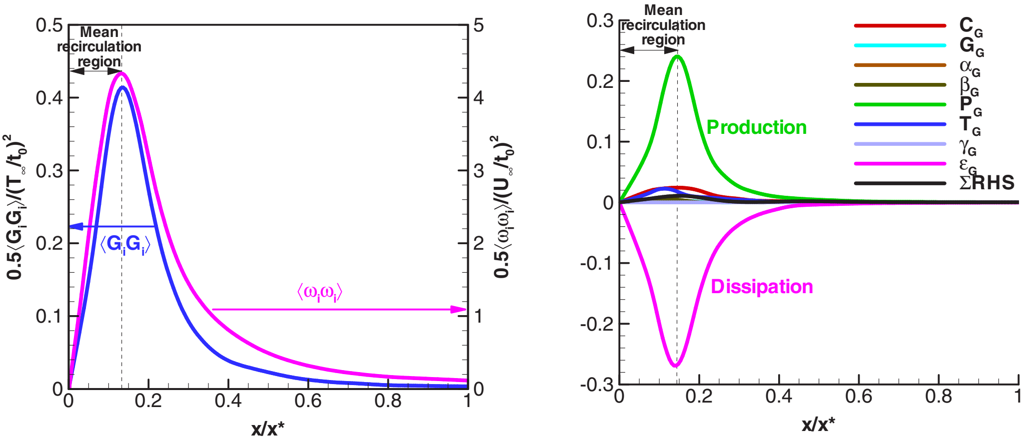

(a)

(b)

FIG. 5. (a) Evolution of scalar-gradient variance and enstrophy along the bar centerline; (b) evolution of budget terms of scalar-gradient variance along the bar centerline. All terms are normalized by $U_\infty T_\infty^2/t_0^3$.

In the present case, the budget analysis reveals that the evolution of scalar-variance along the grid-element centerline is controlled by two terms: turbulent transport and dissipation. Although the turbulent transport of turbulent kinetic energy [also shown in Fig. 4(b)] and that of scalar-variance reach a peak value around $x/x^* \approx 0.3$, their evolution downstream of $x/x^* \approx 0.3$ differs. In particular, the turbulent transport of of scalar-variance is negligible after $x/x^* \approx 0.45$, while that of kinetic energy persists farther downstream. It is interesting to notice that the spatial shape of the two turbulent transport terms shares many similarities with the shape of scalar-variance and kinetic energy. To get a more detailed picture of scalar dynamics for our configuration, in the next section we examine the evolution of scalar-gradient variance.

B. Scalar-gradient variance balance

This subsection focuses on the evolution of the small-scale term, the scalar-gradient variance $\langle G_i G_i\rangle$, where $G_i = \frac{\partial T}{\partial x_i}$. As mentioned earlier, the scalar dissipation ϵ_v is proportional to this term.

Denoting the gradient of instantaneous scalar (i.e., mean plus fluctuation) as $G_i^* = \frac{\partial T^*}{\partial x_i}$, the transport equation can be written as (see Ref. [55])

$$\frac{\partial\left(\left\langle\frac{1}{2}G_iG_i\right\rangle\right)}{\partial t} = \underbrace{-U_j\frac{\partial(\langle G_iG_i\rangle)}{\partial x_j}}_{C_G} \underbrace{-\langle G_iu_j\rangle\left\langle\frac{\partial G_i^*}{\partial x_j}\right\rangle}_{G_G} \underbrace{-\left\langle G_i\frac{\partial u_j}{\partial x_i}\right\rangle\left\langle\frac{\partial G_i^*}{\partial x_j}\right\rangle}_{\alpha_G} \underbrace{-\langle G_iG_j\rangle\frac{\partial U_j}{\partial x_i}}_{\beta_G} \underbrace{-\langle G_is_{ij}G_j\rangle}_{P_G}$$

$$\underbrace{-\frac{1}{2}\frac{\partial}{\partial x_j}\langle G_iG_ju_j\rangle}_{T_G} \underbrace{+\frac{\alpha}{2}\frac{\partial^2}{\partial x_j\partial x_j}(\langle G_iG_i\rangle)}_{D_G} \underbrace{-\alpha\left\langle\frac{\partial G_i}{\partial x_j}\frac{\partial G_i}{\partial x_j}\right\rangle}_{\epsilon_G}, \tag{5}$$

where C_G is the convection by mean flow, G_G and β_G are the production terms by mean scalar and velocity gradient, respectively, α_G is the mixed production, P_G is the production by turbulent stretching and compression, T_G is transport by turbulent fluctuations, D_G is the diffusion, and ϵ_G is the dissipation.

The evolution of scalar-gradient variance along the bar centerline is presented in Fig. 5(a). It is very similar to that of the mean enstrophy, also shown in the figure, with values reaching a peak at the end of the mean recirculation region and then monotonically decaying farther downstream.

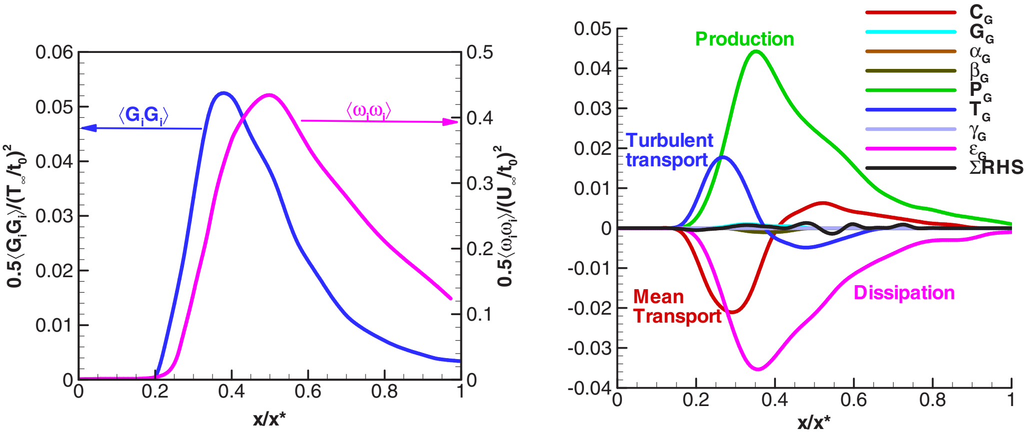

(a)

(b)

FIG. 6. (a) Evolution of scalar-gradient variance and enstrophy along the grid-element centerline; (b) evolution of budget terms of scalar-gradient variance along the grid-element centerline. All the terms are normalized by $U_\infty T_\infty^2/t_0^3$.

The corresponding budget terms, shown in Fig. 5(b), reveal that the growth of $\langle G_i G_i \rangle$ is due to the stretching and compression of the gradient vector G_i by the fluctuating strain field (term P_G). This is balanced by the dissipation throughout the bar centerline, while the contribution of all the other terms is negligible. In the field experiments of Ref. [1], the contribution of mean fields (both velocity and scalar) to the generation of small scales was also found to be negligible.

The spatial evolution of scalar-gradient variance and mean enstrophy, however, differ along the grid-element centerline. As expected, the scalar-gradient variance is negligible in the region upstream the meeting of the wakes. It starts increasing at $x/x^* \approx 0.2$ until $x/x^* \approx 0.4$, and the growth is faster than that of enstrophy [Fig. 6(a)]. Also decay starts earlier compared to enstrophy; this difference is further discussed in Sec. VI.

The budgets along the grid-element centerline are plotted in Fig. 6(b). The first term to initiate the growth of $\langle G_i G_i \rangle$ is the turbulent transport term; this is similar to scalar-variance. Once scalar gradients appear in the centerline, the background strain, which is mainly due to pressure Hessian and turbulent transport [37], activates the production stretching and compression term P_G, which takes over and becomes the main growth mechanism. The two production terms are balanced by mean convection and dissipation. After $x/x^* \approx 0.4$, the mean convection and production are balanced by turbulent transport and dissipation. Far downstream, the transport terms (both mean and turbulent) become negligible, and only the production and dissipation terms remain that balance each other. A more detailed analysis of the production due to stretching and compression is presented in Sec. V.

IV. SPECTRUM OF THE FLUCTUATING SCALAR

Results are presented only along the grid-element centerline. As demonstrated in Sec. III B, the scalar and turbulent kinetic energy dissipation evolve differently along the grid-element centerline, and both intermittent as well as fully turbulent regions exist [see Fig. 2(a)]. As will be shown in this study, scalar gradient dynamics also exhibit intriguing behavior along the grid-element centerline.

The values of the Taylor-scale Reynolds number (Re_λ) and the Corrsin-scale Péclet number (Pe_{λ_T}) at different stations are provided in Table I. Note the low values of Re_λ and Pe_{λ_T}. Such values allow for very well resolved numerical simulation and long time integration, both of which are conducive to the statistical convergence of second and third order correlations as well as good balance of transport equations. In the following we assess whether turbulence properties that are found for high Reynolds

TABLE I. Values of Pe_{λ_T} and Re_λ at different locations along the grid-element centerline. Here $\mathrm{Re}_\lambda = \frac{\lambda}{\nu}\sqrt{\frac{\langle u_i u_i\rangle}{3}}$ where λ is the Taylor microscale defined as $\lambda = \sqrt{\frac{5\nu\langle u_i u_i\rangle}{\epsilon_k}}$ and $\mathrm{Pe}_{\lambda_T} = \frac{\lambda_T}{\alpha}\sqrt{\frac{\langle u_i u_i\rangle}{3}}$ where λ_T is the Corrsin microscale, defined as $\lambda_T = \sqrt{\frac{6\alpha\langle T^2\rangle}{\epsilon_v}}$.

x/x^*	0.1	0.25	0.35	0.5	0.75	0.95
$\mathrm{Pe}_{\lambda T}$	5.21	12.31	19.45	25.6	24.71	23.89
Re_λ	10.21	22.01	34.49	37.58	39.12	33.12

and Péclet number flows can be also detected in flows with low values of these parameters. To this end, we analyze the scalar spectra along the grid-element centerline.

References [10,11] extended the phenomenology of Kolmogorov [56] to the scalar field and developed what is known as Kolmogorov-Obukhov-Corrsin (KOC) theory. It is concerned with locally HIT at very high Reynolds and Péclet numbers. One of its main predictions when $\mathrm{Pr} < 1$ is that a range of wave numbers exists where the scalar spectrum (E_{TT}) takes the form

$$E_{TT}(\kappa) = C_{\epsilon T}\epsilon_k^{-1/3}\epsilon_v\kappa^{-5/3} \tag{6}$$

where $C_{\epsilon T}$ is the Obukhov-Corrsin constant and κ is the wave number. It is important to stress that the claim of KOC theory is that $E_{TT}(\kappa) \sim \kappa^{-5/3}$ is applicable only to fully developed HIT at high Re_λ and Pe_{λ_T}.

The computed and compensated spectra at different locations along the grid-element centerline are illustrated in Fig. 7. At $x/x^* = 0.25$, where the velocity spectrum was reported to exhibit a $-5/3$ slope for the first time along the grid-element centerline (refer to Ref. [37]), the scalar spectrum has a well-defined $-5/3$ slope for about a decade of frequencies [see the compensated spectra for $x/x^* = 0.25$ in Fig. 7(b)]. It is indeed surprising that such a well-defined power-law appears at a location where the local Re_λ and Pe_{λ_T} numbers are too low for an inertial subrange to exist. In fact, Re_λ is only 22.01 and $\mathrm{Pe}_{\lambda T}$ is a mere 12.31 (see Table I). Due to these very small values and the developing nature of the turbulence, the scalar spectrum is not at all expected to have any power-law scaling at this location. Yet the spectrum does exhibit a definite $-5/3$ power-law slope for just under

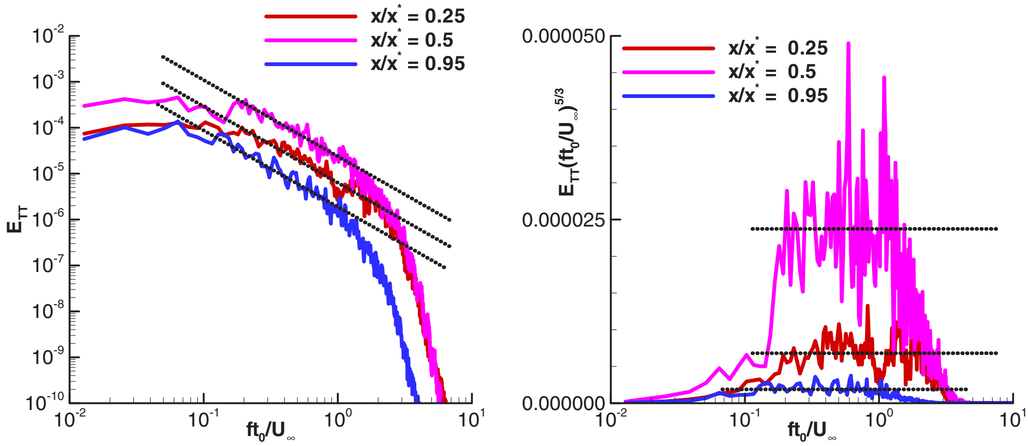

(a)

(b)

FIG. 7. (a) Spectra of the fluctuating scalar at different locations along the grid-element centerline; (b) compensated spectra plotted in linear-logarithmic axes at the same locations. The dotted lines in (a) indicate the $-5/3$ slope, and in (b) they represent a constant value of $E_{TT}(ft_0/U_\infty)^{5/3}$.

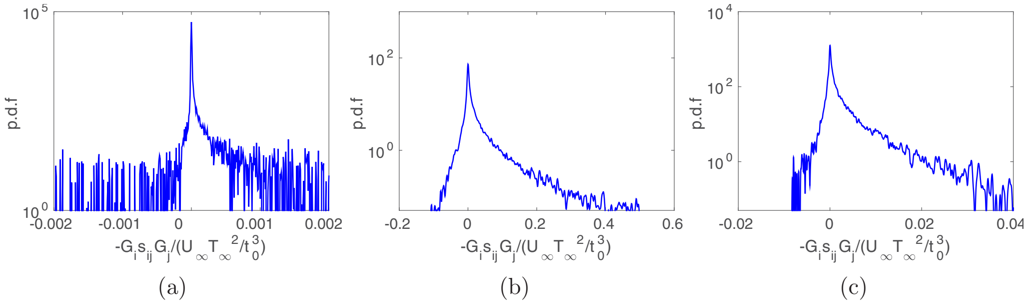

FIG. 8. PDF of scalar gradient production at different locations along the grid-element centerline: (a) $x/x^* = 0.25$, (b) $x/x^* = 0.5$, (c) $x/x^* = 0.95$.

a decade of frequencies. Note also that $x/x^* = 0.25$ is the location where the fluctuating scalar and its gradients have just been brought to the grid-element centerline by the turbulent transport from the bar wakes (see Sec. III).

The power-law behavior observed in the near-grid-element region is not related to the KOC theory. The relationship between the small scales of scalar and the well-defined $-5/3$ power-law slope is further analyzed in Sec. V. Note that this is the first study that reports a well-defined $-5/3$ power-law in the scalar spectrum for a flow characterized by intermittent switching between turbulent and potential flow region at such low overall Re_λ and Pe_{λ_T} numbers.

The scalar spectra in the more homogeneous decay region are also plotted in Figs. 7(a) and 7(b). The frequency range of $-5/3$ slope appears to be decreasing in these locations compared to that of the near-grid-element region. This is consistent with the observations made for the velocity spectra in Ref. [37]. At these fully turbulent locations, Ref. [37] reported that the velocity spectra have power-law slope defined only for a limited range of frequencies. The scalar spectra however have a more clearly defined power-law for a wider range of frequencies. This observation has also been reported in the literature on heated grid fully developed homogeneous turbulence, but for high Re_λ and $\mathrm{Pe}_{\lambda T}$ values [12,27]. The $-5/3$ range of scalar spectra with respect to velocity spectra is also reported in Ref. [57].

V. EIGENCONTRIBUTIONS OF STRAIN RATE TO THE SCALAR GRADIENT PRODUCTION

In this section, we explore further the relation of small scales with the spectra. To this end, the stretching and compressing of the scalar-gradient vector, $-G_is_{ij}G_j$, which is the main production term of scalar dissipation is analyzed. This term can be written as

$$-G_is_{ij}G_j = -|\mathbf{G}|^2\lambda_1\cos^2(\mathbf{G},\mathbf{e_1}) - |\mathbf{G}|^2\lambda_2\cos^2(\mathbf{G},\mathbf{e_2}) - |\mathbf{G}|^2\lambda_3\cos^2(\mathbf{G},\mathbf{e_3}), \tag{7}$$

where $\mathbf{G}$ is the scalar-gradient vector, while λ_i and $\mathbf{e_i}$ (where $i = 1,2,3$) are the strain-rate eigenvalues and eigenvectors, respectively. Equation (7) shows that the production of scalar dissipation depends on the strain-rate eigenvalues and the alignment between the scalar-gradient vector and the strain-rate eigenvectors. The statistical behavior of the production term is discussed first, followed by an analysis of the contribution of the individual eigenvalues and eigenvectors.

The PDFs of scalar gradient production are plotted at different locations in Fig. 8. The PDFs are skewed towards positive at all stations. The positive value of $-\langle G_is_{ij}G_j\rangle > 0$ is considered a universal behavior of small-scale scalar turbulence [1,21,51,58–60]. The same behavior is observed also here, at locations where the local Re_λ is very small and the flow is intermittent.

Table II records the values of production term normalized by the product $\langle s^2\rangle^{1/2} = \langle s_{ij}s_{ij}\rangle^{1/2}$ and $\langle G^2\rangle = \langle G_iG_i\rangle$. This ratio initially increases rapidly from $x/x^* \approx 0.2$ to 0.35. This increase shows that $-\langle G_is_{ij}G_j\rangle$ increases faster than the product $\langle G^2\rangle\langle s^2\rangle^{1/2}$. Farther downstream, the ratio decreases gradually. This is because $\langle s^2\rangle$ increases slightly in this region (i.e., from $x = 0.35x^*$ to

TABLE II. Values of normalized stretching and compressing at different locations along the grid-element centerline.

x/x^*	0.1	0.25	0.35	0.5	0.75	0.95
$-\langle G_i s_{ij} G_j\rangle/\langle G^2\rangle\langle s^2\rangle^{1/2}$	–	0.11	0.195	0.19	0.18	0.17

$0.5x^*$; see Fig. 10 of Ref. [37]). Far downstream the ratio again decreases slowly, ascertaining that the decay of $-\langle G_i s_{ij} G_j\rangle$ is similar to that of $\langle G^2\rangle$ and $\langle s^2\rangle^{1/2}$. Therefore, the growth of $-\langle G_i s_{ij} G_j\rangle$ is faster than $\langle s^2\rangle^{1/2}\langle G^2\rangle$, while its decay is similar to that of $\langle s^2\rangle^{1/2}\langle G^2\rangle$. The reason for this behavior will become clearer later in this section.

A. The role of strain-rate eigenvalues in scalar gradient production

The strain-rate eigenvalues are ordered as $\lambda_1 > \lambda_2 > \lambda_3$. The incompressibility constraint implies that $\lambda_1 + \lambda_2 + \lambda_3 = 0$. The largest strain-rate eigenvalue is always positive (i.e., $\lambda_1 > 0$), and the third eigenvalue is always negative (i.e., $\lambda_3 < 0$). The intermediate eigenvalue can be either positive or negative. For many turbulent flows, the intermediate eigenvalue is positive on average, and this is one of the universal properties of small-scale turbulence [16,39,61,62]. These strain-rate eigenvalues influence the scalar gradient production as indicated in Eq. (7) (refer also to Ref. [1]). It is known from Ref. [37] that in the grid-element centerline region $0.25 < x/x^* < 1$, the PDF of the intermediate strain-rate eigenvalue is skewed positive resulting in two stretching directions and one compressive direction. More statistics of the normalized strain-rate eigenvalues are provided in Table III. The normalized values of $\langle\lambda_i^2\rangle$ (where $i = 1,2,3$) remain remarkably constant, while the normalized values of $\langle\lambda_1\rangle$ and $\langle\lambda_3^3\rangle$ increase and $\langle\lambda_1^3\rangle$ and $\langle\lambda_3\rangle$ values decrease. The downstream evolution of $\langle\lambda_2\rangle$, $\langle\lambda_2^2\rangle$, and $\langle\lambda_2^3\rangle$ remains insensitive to any kind of normalization, although the PDF of λ_2 showed remarkable difference from the near-grid element to the decay regions as reported in Ref. [37]. In Table III, the values from an atmospheric boundary layer field experiment [63] are also provided. Although the Reynolds number of the field experiment is too large ($\mathrm{Re}_\lambda \approx 10^4$), the computed values of normalized mean strain-rate eigenvalues are surprisingly close, in particular for $\langle\lambda_i\rangle$ and $\langle\lambda_i^2\rangle$.

We turn now our attention to the contribution of the strain-rate eigenvalues on the scalar gradient production. Figure 9 shows the joint probability distribution (JPDF) between the strain-rate eigenvalues and the scalar gradient production. The analysis is carried out at two stations along the grid-element centerline: (1) at $x/x^* = 0.25$ located in the near-grid-element region [Figs. 9(a)–9(c)]

TABLE III. Values of normalized eigenvalues of strain-rate tensor at different locations along the grid-element centerline. The values are compared against the field experiments of Ref. [1].

Quantity: x/x^*	0.1	0.25	0.35	0.5	0.75	0.95	Field experiment
$\langle\lambda_1\rangle/\langle s^2\rangle^{\frac{1}{2}}$	–	0.40	0.48	0.54	0.55	0.56	0.53
$\langle\lambda_2\rangle/\langle s^2\rangle^{\frac{1}{2}}$	–	0.09	0.09	0.12	0.13	0.13	0.09
$\langle\lambda_3\rangle/\langle s^2\rangle^{\frac{1}{2}}$	–	−0.49	−0.57	−0.66	−0.68	−0.69	−0.62
$\langle\lambda_1^2\rangle/\langle s^2\rangle$	–	0.36	0.38	0.37	0.36	0.36	0.4
$\langle\lambda_2^2\rangle/\langle s^2\rangle$	–	0.05	0.05	0.05	0.05	0.05	0.04
$\langle\lambda_3^2\rangle/\langle s^2\rangle$	–	0.59	0.57	0.58	0.59	0.59	0.56
$\langle\lambda_1^3\rangle/\langle s^2\rangle^{\frac{3}{2}}$	–	0.74	0.43	0.32	0.28	0.28	0.48
$\langle\lambda_2^3\rangle/\langle s^2\rangle^{\frac{3}{2}}$	–	0.05	0.02	0.02	0.05	0.05	0.01
$\langle\lambda_3^3\rangle/\langle s^2\rangle^{\frac{3}{2}}$	–	−1.57	−0.86	−0.66	−0.60	−0.60	−0.73

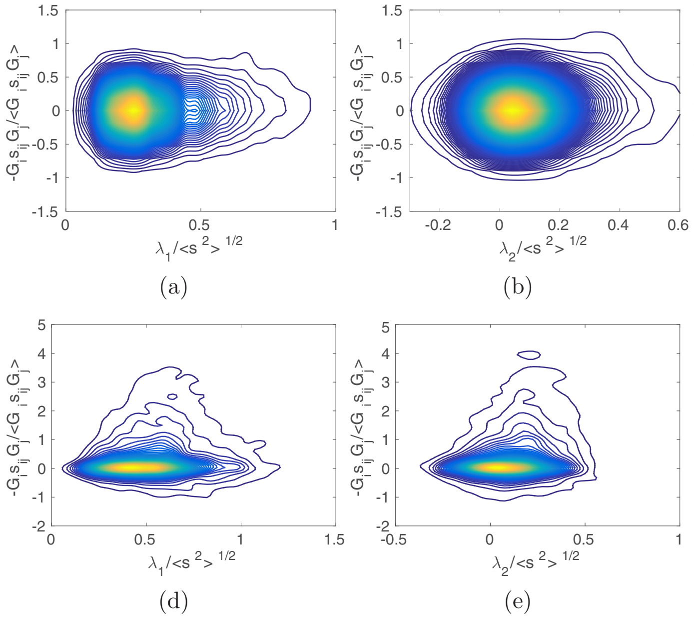

FIG. 9. JPDF of eigenvalues of strain-rate tensor against the scalar gradient production: (a)–(c) at $x/x^* = 0.25$ (near-grid-element inhomogeneous region), (d)–(f) at $x/x^* = 0.95$ (decay region). The isocontours range from 10^1 to 10^{-1}.

and (2) at $x/x^* = 0.95$ located in the far-downstream decay region [Figs. 9(d)–9(f)]. Figures 9(d)–9(f) also look similar to those reported in Gulitski *et al.* [63] (see Fig. 16 of their paper) for the atmospheric boundary layer. It is evident from Fig. 9 that the extensive λ_1 and compressive λ_3 strain-rate eigenvalues are positive and negative, respectively, while the tendency for the intermediate strain-rate eigenvalue λ_2 to skew towards positive is apparent in both the near-grid element and far-downstream regions.

The preference for the positive scalar gradient production is marginal only at a location where the scalar spectrum exhibits the best $-5/3$ power-law slope. Since stretching and compression are believed to have a close relationship with the scalar cascade, it might be intuitive to expect a stronger preference for the production term of scalar gradients, but in reality that does not occur. This indicates that the stretching and compression process of scalar gradients may not be the most fundamental process behind the $-5/3$ power-law slope. This is further ascertained in Figs. 9(d)–9(f) where the production of scalar gradient is strongly preferred (as evident from the asymmetry in the JPDF with respect to $-G_is_{ij}G_j/\langle G_is_{ij}G_j\rangle = 0$), yet the spectrum at this location has a power-law defined for a more narrow range of frequencies than that of the near-grid-element region. Figures 9(d)-9(f) also reveal that there is a correlation between the strain-rate eigenvalues and the positive skewness of scalar gradient production in the homogeneous decay region.

B. The role of geometrical alignments in scalar gradient production

The other factor that affects the production of scalar gradient, the geometrical alignments [refer to Eq. (7)], is analyzed in this subsection. These alignments were first reported in Ref. [16] for a periodic homogeneous isotropic turbulence. It was observed that the fluctuating scalar-gradient vector aligns with the compressive strain-rate eigenvector, and it is perpendicular to the intermediate strain-rate eigenvector. The extensive strain-rate eigenvector aligns 45° with the fluctuating scalar-gradient vector. These observations were also verified in subsequent studies of Refs. [1,17,21]. These alignment properties are also considered universal characteristics of small-scale scalar turbulence.

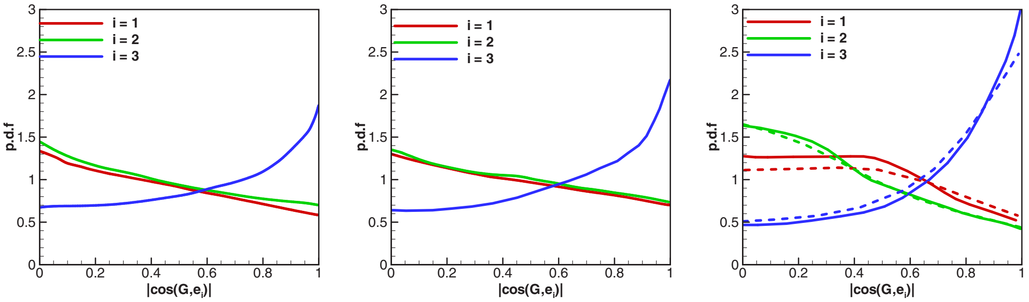

(a) (b) (c)

FIG. 10. PDF of cosine of the angle between scalar-gradient vector and strain-rate eigenvectors at different locations along the grid-element centerline: (a) $x/x^* = 0.25$, (b) $x/x^* = 0.35$, (c) $x/x^* = 0.5$. The dotted lines in (c) are the results from Ref. [21].

The PDFs of the absolute value of the cosine of the angle between the fluctuating scalar-gradient vector and the strain-rate eigenvectors are plotted for different grid-element centerline locations in Fig. 10. The alignment behavior at $x/x^* = 0.25$ and 0.35 is shown in Figs. 10(a) and 10(b), respectively. The scalar-gradient vector aligns with the compressive strain-rate eigenvector but is normal to the other two eigenvectors. This is not the universal alignment behavior reported in the previous studies [1,17,21]. Note that at the same locations the alignment behavior of vorticity was also found in Ref. [37] to be anomalous; the vorticity vector aligned with both the extensive and intermediate strain-rate eigenvectors. Note also that the alignment of the compressive strain-rate eigenvector with the scalar-gradient vector becomes stronger from $x/x^* = 0.25$ to 0.35 giving a possible answer as to why the scalar-gradient-variance increase in the region $0.2 < x/x^* < 0.35$ [refer to Fig. 6(a)]. The alignment behavior for the region $0.2 < x/x^* < 0.35$ agrees with the results of Ref. [60], which reported that strain-dominated regions strengthen the alignment of the scalar-gradient vector with the compressive strain-rate eigenvector. The alignment behavior after $x/x^* \approx 0.4$ starts to exhibit the universal trend reported in the literature as the PDFs in Fig. 10(c), plotted for $x/x^* = 0.5$, are very similar to the results of Ref. [21]. This universal alignment behavior prevails throughout the decay region although the values of Pe_{λ_T} and Re_λ are significantly low.

Unlike the alignment behavior of the fluctuating scalar-gradient vector with the strain-rate eigenvectors that changes along the grid-element centerline, the alignment with the fluctuating vorticity vector remains the same as noted in Fig. 11(a). The figure also shows that homogeneity in

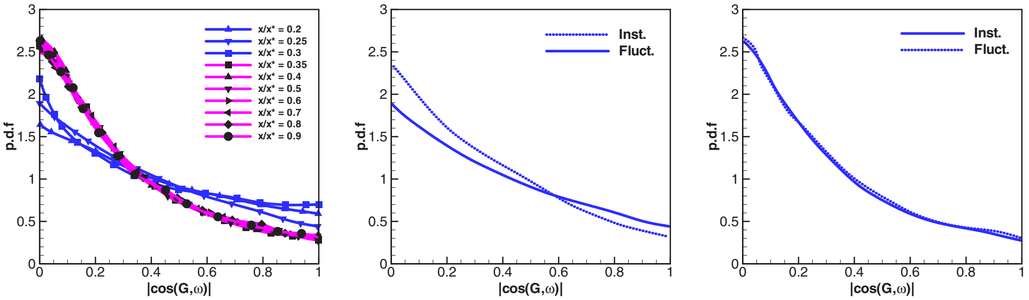

(a) (b) (c)

FIG. 11. (a) PDF of cosine of the angle between fluctuating scalar gradient and vorticity vectors at different locations along the grid-element centerline; (b), (c) comparison between alignments of instantaneous versus fluctuating scalar gradient and vorticity vectors at (b) $x/x^* = 0.25$, (c) $x/x^* = 0.5$.

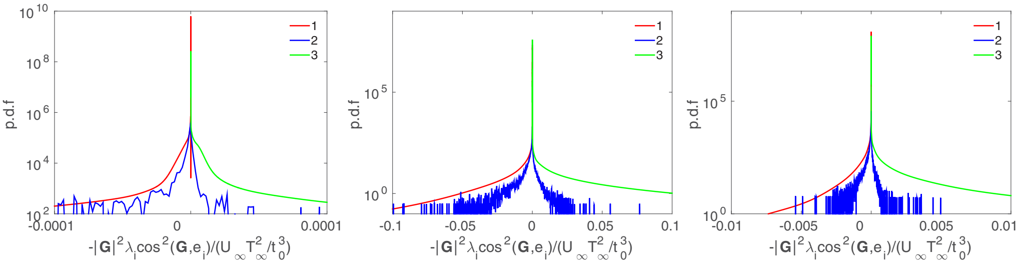

(a) (b) (c)

FIG. 12. PDF of eigencontribution to scalar gradient production at different locations along the grid-element centerline: (a) $x/x^* = 0.25$, (b) $x/x^* = 0.5$, (c) $x/x^* = 0.95$.

fluctuating vorticity statistics is attained only in the downstream of $x/x^* \approx 0.35$. The fluctuating scalar-gradient vector aligns perpendicular to the vorticity vector throughout the grid-element centerline. This result closely follows the mathematical fact that the instantaneous scalar product between vorticity and scalar-gradient vectors is a Lagrangian inviscid invariant. We also noted some difference between instantaneous and fluctuating alignment characteristics of scalar-gradient and vorticity vectors only in the inhomogeneous region where the mean gradients are strong [see Fig. 11(b)]. On the other hand, the alignments results of instantaneous and fluctuating scalar-gradient and vorticity vectors are nearly similar in the homogeneous region starting from $x/x^* \approx 0.5$ as shown in Fig. 11(c).

C. The combined effects of strain-rate eigenvalues and eigenvectors to scalar gradient production

The combined effect of strain-rate eigenvalues and eigenvectors on the scalar gradient production is plotted in Fig. 12. At $x/x^* = 0.25$, where the scalar-gradient variance has just started to develop and the scalar spectrum has the best-defined $-5/3$ power-law slope, the production of scalar gradient is predominantly due to the compressive strain-rate eigenvalue and eigenvector as only the PDF of $-|\mathbf{G}|^2\lambda_3 \cos^2(\mathbf{G},\mathbf{e_3})$ is skewed to the positive. A similar finding was reported in Ref. [1] but for a homogeneous isotropic turbulence. Therefore, the small scales of scalar are due to compressing of fluid elements, although the small scales of velocity fluctuation are due to vortex stretching. As a novelty, this study takes this result one step further and shows that this compressing of fluid elements is mostly associated with the strain-rate eigenvectors for the developing inhomogeneous turbulence. In the decay region, some portion of the PDF of $-|\mathbf{G}|^2\lambda_2 \cos^2(\mathbf{G},\mathbf{e_2})$ is in the positive x axis, but the overall contribution is negative.

The observations noted in Fig. 12 are further analyzed through the mean values of individual components of the eigencontribution to the scalar gradient production (see Table IV). The values of $\langle|\mathbf{G}|^2\lambda_1 \cos^2(\mathbf{G},\mathbf{e_1})\rangle$ and $\langle|\mathbf{G}|^2\lambda_2 \cos^2(\mathbf{G},\mathbf{e_2})\rangle$ are negative, and the only positive component is $\langle|\mathbf{G}|^2\lambda_3 \cos^2(\mathbf{G},\mathbf{e_3})\rangle$. This observation ascertains that the production of scalar gradient is due to the compressive action of strain-rate eigenvalues and eigenvectors [1]. The mean eigencontribution values are compared against the very high Reynolds number field experiments of Ref. [1]. Although

TABLE IV. Contribution of strain-rate eigenvalues to scalar gradient production. The values are compared with the field experiments of Ref. [1].

Quantity: x/x^*	0.1	0.25	0.35	0.5	0.75	0.95	Field experiment
$\langle\lvert\mathbf{G}\rvert^2\lambda_1 \cos^2(\mathbf{G},\mathbf{e_1})\rangle/\langle G_i s_{ij} G_j\rangle$	–	−0.18	−0.31	−0.27	−0.25	−0.22	−0.64
$\langle\lvert\mathbf{G}\rvert^2\lambda_2 \cos^2(\mathbf{G},\mathbf{e_2})\rangle/\langle G_i s_{ij} G_j\rangle$	–	−0.03	−0.04	−0.04	−0.04	−0.04	−0.05
$\langle\lvert\mathbf{G}\rvert^2\lambda_3 \cos^2(\mathbf{G},\mathbf{e_3})\rangle/\langle G_i s_{ij} G_j\rangle$	–	1.21	1.35	1.31	1.29	1.26	1.69

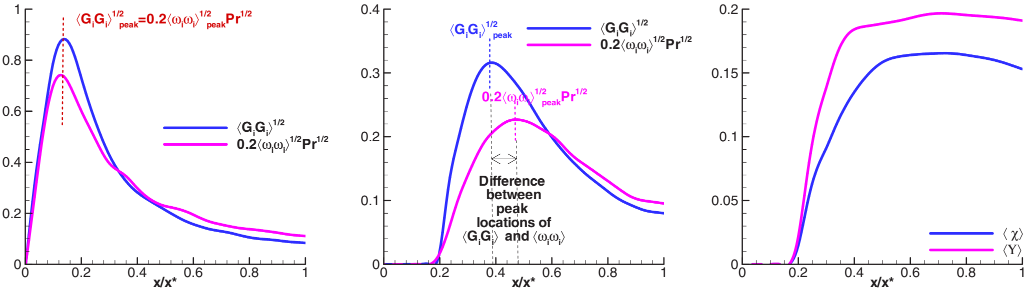

(a) (b) (c)

FIG. 13. Evolution of turbulent kinetic energy and scalar-variance dissipations along (a) the bar centerline and (b) the grid-element centerline. (c) Evolution of the time-averaged quantities χ and Υ (defined in the text) along the grid-element centerline.

the values of $\langle|\mathbf{G}|^2\lambda_2\cos^2(\mathbf{G},\mathbf{e_2})\rangle$ and $\langle|\mathbf{G}|^2\lambda_3\cos^2(\mathbf{G},\mathbf{e_3})\rangle$ are closer to the literature values, the values of $\langle|\mathbf{G}|^2\lambda_1\cos^2(\mathbf{G},\mathbf{e_1})\rangle$ show some significant discrepancy. Recall that the present simulation is carried out for a low Reynolds number, and the observed discrepancy could well be a Reynolds number effect.

Concerning the evolution of $\langle|\mathbf{G}|^2\lambda_3\cos^2(\mathbf{G},\mathbf{e_3})\rangle$ with respect to $-\langle G_i s_{ij} G_j\rangle$, it can be noted that the behavior of these two terms are similar; both terms increase from $x/x^* = 0.2$ to 0.4, and then they decay gradually. Noting from Table III that the values of $\langle\lambda_3\rangle$ decrease from $x = 0.25x^*$ to $0.4x^*$, the rapid increase of $-\langle G_i s_{ij} G_j\rangle$ compared to $\langle G_i G_i\rangle$ and $\langle s_{ij}s_{ij}\rangle$ is the result of rapid increase in the strong alignment between the compressive strain-rate eigenvector and the scalar-gradient vector. In simple terms, the asymmetric evolution of $-\langle G_i s_{ij} G_j\rangle$ compared to $\langle G_i G_i\rangle$ and $\langle s_{ij}s_{ij}\rangle$ is the result of asymmetric evolution of the alignment behavior between the strain-rate eigenvector and the scalar-gradient vector.

VI. STRETCHING OF THE VORTICITY VECTOR VERSUS STRETCHING OF A PASSIVE VECTOR

The aim of this final section is to provide an explanation as to why the scalar dissipation ($\epsilon_v = \alpha\langle G_i G_i\rangle$) starts decaying earlier along the grid-element centerline compared to kinetic energy dissipation ($\nu\langle\omega_i\omega_i\rangle$), as demonstrated in Fig. 6(a). The dissipation quantities are sometimes believed to have similar behavior [46], and the relationship is given as $\langle G_i G_i\rangle^{1/2} = C\langle\omega_i\omega_i\rangle^{1/2}\mathrm{Pr}^{1/2}$, where C is a constant that depends on the flow conditions. In periodic box simulation, Ref. [19] found that this relation is very well satisfied, with a value of constant C close to 2.

The spatial evolution of these two dissipation rates along the bar and the grid-element centerlines is plotted in Figs. 13(a) and 13(b), respectively. The relationship $\langle G_i G_i\rangle^{1/2} \sim \langle\omega_i\omega_i\rangle^{1/2}\mathrm{Pr}^{1/2}$ is valid only along the bar centerline and for $x/x^* > 0.6$ on the grid-element centerline. Indeed, Fig. 13(a) demonstrates that the qualitative behavior of the two dissipation profiles is similar along the bar centerline, with values peaking at the same position. The value of the constant C in the current simulation is approximately 0.2. At the grid-element centerline, however, the onset of scalar dissipation decay occurs earlier than the decay of kinetic energy dissipation [see Figs. 13(b) and 6(a)]. A similar behavior between the dissipation rates of kinetic energy and scalar-variance is also reported in Refs. [53,54].

In order to provide an explanation for the aforementioned behavior, we explore below in more detail the turbulent stretching and compression of the vorticity and the scalar-gradient vectors. This is motivated by the fact that the dominant production terms are $-G_i s_{ij} G_j$ and $\omega_i s_{ij}\omega_j$, respectively. As noted in Ref. [51], the vorticity vector and turbulent strain rate are coupled. It can be seen from the governing equations of enstrophy ($\omega_i\omega_i$) and strain product ($s_{ij}s_{ij}$) [refer to Eqs. (5.4) and (5.7)

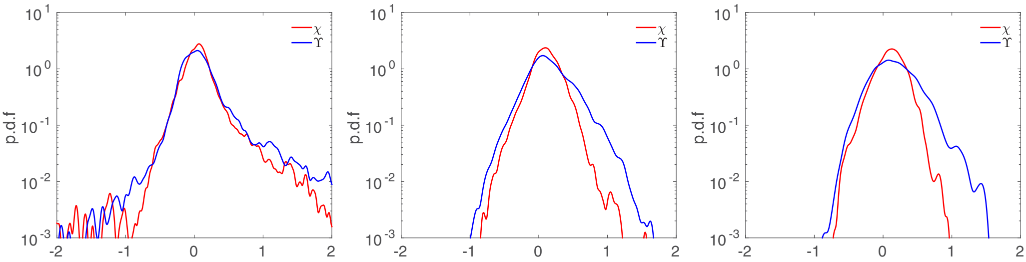

(a) (b) (c)

FIG. 14. PDF of scalar gradient production rate and enstrophy production rate at different locations along the grid-element centerline: (a) $x/x^* = 0.25$, (b) $x/x^* = 0.5$, (c) $x/x^* = 0.95$.

in Ref. [37]] that the vortex stretching and compression term appears in both equations: as a source term for enstrophy and a sink for strain product. This means that the growth of enstrophy reduces the strain rate and thus weakening the stretching and compression, which eventually leads to the enstrophy damping. On the other hand, the stretching of the scalar-gradient vector is determined by strain only (i.e., does not react back). It is thus expected that the statistics of the stretching and compression of the two vectors will be different.

In Ref. [64], the normalized stretching and compression rates of vorticity and scalar gradient were defined as $\chi = \frac{\omega_i s_{ij}\omega_j/\omega_i\omega_i}{\sqrt{\langle\omega_i\omega_i\rangle}}$ and $\Upsilon = \frac{-G_i s_{ij} G_j/G_i G_i}{\sqrt{\langle\omega_i\omega_i\rangle}}$. The variation of χ and Υ along the different grid-element centerline is shown in Fig. 13(c). Clearly, the stretching and compression rate of the passive vector is stronger than that of the vorticity vector throughout the grid-element centerline (see Fig. 14). The dominance of passive vector stretching and compression over the vorticity vector was first reported in Ref. [64]. The current results, however, cannot be directly compared with [64], as the latter considers "frozen" passive vectors that satisfy the continuity equation. For the distinction between the two types of passive vectors refer to Ref. [51].

The reason for the observed difference lies in the two-way coupling between strain and vorticity. When the mean enstrophy increases in the region of $0.2 < x/x^* < 0.5$ [see Fig. 8(a) of Ref. [37]], the stretching of vorticity also increases in this region, but this increase weakens the strain-rate magnitude (because the stretching and compression term acts as a sink for the strain), which in turn reduces the strength of vortex stretching and compression (that depends on the strain magnitude). This can explain why the stretching and compression rate of vorticity vector is smaller than that of a passive vector. Although the comparison of stretching and compression rates between the vorticity vector and the scalar-gradient vector confirms the validity of Ohkitani's observation for the current case, it cannot explain why the onset of scalar-variance dissipation decay occurs much earlier along the grid-element centerline.

Figure 13(c) demonstrates that the growth of both χ and Υ is suddenly hampered. This occurs earlier for the passive scalar field compared to the vorticity field. What is the process that suddenly impedes the growth of stretching and compression rates? It is intuitive that this process should be related to the stretching and compression term. Indeed, as shown in the next paragraph, the decay of scalar dissipation starts earlier than that of the kinetic energy dissipation due to the difference in alignments between the scalar-gradient vector and the strain-rate eigenvector. The production of the two dissipation quantities depends on the strain-rate eigenvalues and the alignment of the eigenvectors with the vorticity and scalar-gradient vector [Eq. (7)]. Since the strain-rate eigenvalues appear in the same way in both production terms, the difference in evolution should originate from the geometrical alignments.

For the kinetic energy dissipation, the extensive and intermediate eigenvectors aid the growth of $\langle\omega_i\omega_i\rangle$ (see Fig. 20 of Ref. [37]). On the other hand, as reported in many studies (and confirmed in Fig. 12), the growth of $\langle G_i G_i\rangle$ occurs predominantly due to the compressive eigenvector.

This is because, as was noticed earlier, the extensive eigenvector has a negative effect on the growth of scalar-gradient variance, and the intermediate eigenvector aligns perpendicular to the scalar-gradient vector. The vorticity vector aligns with both the extensive and intermediate eigenvectors in the region $0.2 < x/x^* \leqslant 0.5$, and thus acting as a main agent to increase $\langle \omega_i \omega_i \rangle$ in that region (see Fig. 22 of Ref. [37]). If $\langle G_i G_i \rangle$ has to increase in $0.2 < x/x^* \leqslant 0.5$, then the scalar-gradient vector is expected to align only with the compressive eigenvector. Yet such an alignment behavior is noticed only in the region $0.2 < x/x^* < 0.4$ where the extensive and intermediate eigenvectors align perpendicular to the scalar-gradient vector, and thus they do not hamper the growth of scalar-gradient variance due to the compressive eigenvector. When the extensive strain-rate eigenvector aligns 45° to the scalar-gradient vector (i.e., after $x/x^* > 0.4$), the negative effect due to this alignment on the scalar-gradient variance is felt in the form of decreasing the scalar-gradient variance. Comparing the alignment behavior of the scalar-gradient vector with that of the vorticity vector, it is observed that the vorticity vector changes its alignment behavior later along the grid-element centerline (it occurs only after $x/x^* = 0.5$) than that of the scalar-gradient vector. Thus, the delayed change in alignment behavior of vorticity vector causes the scalar-variance dissipation to decay earlier along the grid-element centerline than the turbulent kinetic energy dissipation.

VII. CONCLUSIONS

This paper presents a statistical analysis of a passive scalar (in the form of temperature) injected into a spatially developing turbulence. The turbulence is generated by a single square grid element which is heated continuously. The main objective of this study was to seek answers to the five questions raised in Sec. I. The answers for those questions are given below:

(1) The large-scale quantity (scalar-variance) is generated mainly behind the bars due to the action of mean scalar gradients. It is then laterally transported to the grid-element centerline through turbulent transport due to the intermittent meeting of the bar wakes (external intermittency). The mean velocity and scalar fields have a minimal effect on the production of the small-scale quantity (scalar-gradient variance, proportional to scalar dissipation), even behind the grid-element bars. Instead, this is produced by the turbulent strain rate via the stretching and compressing process. This study has shown that the production of scalar dissipation is due to compressive action of strain rate, while it is the stretching action that produces the kinetic energy dissipation.

(2) Although the evolution of scalar dissipation is similar to the turbulent kinetic energy dissipation along the bar-centerline, they behave differently along the grid-element centerline. The different alignment behavior of the scalar-gradient vector and the vorticity vector with the strain-rate eigenvectors explains why the scalar dissipation decays much earlier along the grid-element centerline than that of the turbulent kinetic energy dissipation.

(3) The scalar spectrum is observed to exhibit the best $-5/3$ power-law slope in the near-grid-element region. This slope occurs even in the highly intermittent, non-Gaussian and inhomogeneous region where the local Re_λ and Pe are significantly low.

(4) The $-5/3$ slope in the scalar spectrum is most clearly observed in the regions where the small-scale terms of scalar have just started developing. The scalar spectrum has a well-defined $-5/3$ power-law slope for at least a decade of frequencies in the locations where the strength of stretching and compressing of scalar gradient by strain rate is weak. On the other hand, in the locations where the stretching and compressing strength is high, the frequency range becomes narrower. Hence, the stretching and compressing process of scalar gradients by strain rate (equivalent to the vortex stretching process in velocity field) is not necessarily the cause of the $-5/3$ power-law behavior.

(5) Moving from the near-grid-element centerline region to far downstream, it is noted that the $-5/3$ slope in the scalar spectrum slowly erodes, and the alignment between the scalar-gradient vector and the strain-rate eigenvector morphs into the universal alignment behavior reported in the literature.

ACKNOWLEDGMENTS

This research project was funded by the European Commission under the Innovative Doctoral Program (IDP) in Marie Curie framework through MULTISOLVE (Grant Agreement Number 317269). The simulations were carried out on the facilities of Archer, the UK national high-performance computing service under the grant EP/L000261/1 of the UK Turbulence Consortium (UKTC), and the High Performance Computing Service of Imperial College London. J.C.V. acknowledges support from ERC Advanced Grant 320560.

[1] G. Gulitski, M. Kholmyansky, W. Kinzelbach, B. Lüthi, A. Tsinober, and S. Yorish, Velocity and temperature derivatives in high-Reynolds-number turbulent flows in the atmospheric surface layer. Part 3. Temperature and joint statistics of temperature and velocity derivatives, J. Fluid Mech. **589**, 103 (2007).

[2] K. R. Sreenivasan, On local isotropy of passive scalars in turbulent shear flows, Proc. R. Soc. Lond. A **434**, 165 (1991).

[3] K. R. Sreenivasan and R. A. Antonia, The phenomenology of small-scale turbulence, Annu. Rev. Fluid Mech. **29**, 435 (1997).

[4] A. J. Majda and P. R. Kramer, Simplified models for turbulent diffusion: Theory, numerical modelling, and physical phenomena, Phys. Rep. **314**, 237 (1999).

[5] B. I. Shraiman and E. D. Siggia, Scalar turbulence, Nature (London) **405**, 639 (2000).

[6] Z. Warhaft, Passive scalars in turbulent flows, Annu. Rev. Fluid Mech. **32**, 203 (2000).

[7] G. Falkovich, K. Gawędzki, and M. Vergassola, Particles and fields in fluid turbulence, Rev. Mod. Phys. **73**, 913 (2001).

[8] P. E. Dimotakis, Turbulent mixing, Annu. Rev. Fluid Mech. **37**, 329 (2005).

[9] T. Gotoh and P. K. Yeung, Passive scalar transport in turbulence, in *Ten Chapters in Turbulence*, edited by Y. Kaneda, P. A Davidson, and K. R. Sreenivasan (Cambridge University Press, Cambridge, UK, 2013).

[10] A. M. Obukhov, Structure of the temperature field in turbulent flows, Izv. Akad. Nauk SSSR Geogr. Geophys **13**, 58 (1968).

[11] S. Corrsin, On the spectrum of isotropic temperature fluctuations in an isotropic turbulence, J. App. Phys. **22**, 469 (1951).

[12] Z. Warhaft and J. L. Lumley, An experimental study of the decay of temperature fluctuations in grid-generated turbulence, J. Fluid Mech. **88**, 659 (2006).

[13] K. R. Sreenivasan and R. A. Antonia, Skewness of temperature derivatives in turbulent shear flows, Phys. Fluids **20**, 1986 (1977).

[14] K. R. Sreenivasan, R. A. Antonia, and D. Britz, Local isotropy and large structures in a heated turbulent jet, J. Fluid Mech. **94**, 745 (2006).

[15] R. A. Antonia and C. W. Van Atta, On the correlation between temperature and velocity dissipation fields in a heated turbulent jet, J. Fluid Mech. **67**, 273 (2006).

[16] W. M. T. Ashurst, A. R. Kerstein, R. M. Kerr, and C. H. Gibson, Alignment of vorticity and scalar gradient with strain rate in simulated Navier–Stokes turbulence, Phys. Fluids **30**, 2343 (1987).

[17] H. Abe, R. A. Antonia, and H. Kawamura, Correlation between small-scale velocity and scalar fluctuations in a turbulent channel flow, J. Fluid Mech. **627**, 1 (2009).

[18] H. Abe and R. A. Antonia, Scaling of normalized mean energy and scalar dissipation rates in a turbulent channel flow, Phys. Fluids **23**, 055104 (2011).

[19] A. Pumir, A numerical study of the mixing of a passive scalar in three dimensions in the presence of a mean gradient, Phys. Fluids **6**, 2118 (1994).

[20] M. Holzer and E. D. Siggia, Turbulent mixing of a passive scalar, Phys. Fluids **6**, 1820 (1994).

[21] P. Vedula, P. K. Yeung, and R. O. Fox, Dynamics of scalar dissipation in isotropic turbulence: A numerical and modeling study, J. Fluid Mech. **433**, 29 (2001).

[22] K. R. Sreenivasan, S. Tavoularis, R. Henry, and S. Corrsin, Temperature fluctuations and scales in grid-generated turbulence, J. Fluid Mech. **100**, 597 (2006).

[23] C. Tong and Z. Warhaft, On passive scalar derivative statistics in grid turbulence, Phys. Fluids **6**, 2165 (1994).

[24] R. Budwig, S. Tavoularis, and S. Corrsin, Temperature fluctuations and heat flux in grid-generated isotropic turbulence with streamwise and transverse mean-temperature gradients, J. Fluid Mech. **153**, 441 (2006).

[25] L. Mydlarski and Z. Warhaft, Passive scalar statistics in high-Péclet-number grid turbulence, J. Fluid Mech. **358**, 135 (1998).

[26] Jayesh, C.Tong, and Z. Warhaft, On temperature spectra in grid turbulence, Phys. Fluids **6**, 306 (1994).

[27] T. T. Yeh and C. W. Atta, Spectral transfer of scalar and velocity fields in heated-grid turbulence, J. Fluid Mech. **58**, 233 (2006).

[28] R. A. Antonia, S. K. Lee, L. Djenidi, P. Lavoie, and L. Danaila, Invariants for slightly heated decaying grid turbulence, J. Fluid Mech. **727**, 379 (2013).

[29] R. E. Seoud and J. C. Vassilicos, Dissipation and decay of fractal-generated turbulence, Phys. Fluids **19**, 105108 (2007).

[30] N. Mazellier and J. C. Vassilicos, Turbulence without Richardson–Kolmogorov cascade, Phys. Fluids **22**, 075101 (2010).

[31] P. C. Valente and J. C. Vassilicos, The decay of turbulence generated by a class of multiscale grids, J. Fluid Mech. **687**, 300 (2011).

[32] R. Gomes-Fernandes, B. Ganapathisubramani, and J. C. Vassilicos, Particle image velocimetry study of fractal-generated turbulence, J. Fluid Mech. **711**, 306 (2012).

[33] P. C. Valente and J. C. Vassilicos, Universal Dissipation Scaling for Nonequilibrium Turbulence, Phys. Rev. Lett. **108**, 214503 (2012).

[34] Y. Zhou, K. Nagata, Y. Sakai, H. Suzuki, Y. Ito, O. Terashima, and T. Hayase, Development of turbulence behind the single square grid, Phys. Fluids **26**, 045102 (2014).

[35] Y. Zhou, K. Nagata, Y. Sakai, Y. Ito, and T. Hayase, Enstrophy production and dissipation in developing grid-generated turbulence, Phys. Fluids **28**, 025113 (2016).

[36] Y. Zhou, K. Nagata, Y. Sakai, Y. Ito, and T. Hayase, Spatial evolution of the helical behavior and the $2/3$ power-law in single-square-grid-generated turbulence, Fluid Dyn. Res. **48**, 021404 (2016).

[37] I. Paul, G. Papadakis, and J. C. Vassilicos, Genesis and evolution of velocity gradients in near-field spatially developing turbulence, J. Fluid Mech. **815**, 295 (2017).

[38] S. Laizet, J. C. Vassilicos, and C. Cambon, Interscale energy transfer in decaying turbulence and vorticity–strain-rate dynamics in grid-generated turbulence, Fluid Dyn. Res. **45**, 061408 (2013).

[39] R. Gomes-Fernandes, B. Ganapathisubramani, and J. C. Vassilicos, Evolution of the velocity-gradient tensor in a spatially developing turbulent flow, J. Fluid Mech. **756**, 252 (2014).

[40] S. Laizet, J. Nedić, and J. C. Vassilicos, The spatial origin of $-5/3$ spectra in grid-generated turbulence, Phys. Fluids **27**, 065115 (2015).

[41] H. Suzuki, K. Nagata, Y. Sakai, and T. Hayase, Direct numerical simulation of turbulent mixing in regular and fractal grid turbulence, Phys. Scr. **2010**, 014065 (2010).

[42] H. Suzuki, K. Nagata, Y. Sakai, and R. Ukai, High-Schmidt-number scalar transfer in regular and fractal grid turbulence, Phys. Scr. **2010**, 014069 (2010).

[43] S. Laizet and J. C. Vassilicos, Stirring and scalar transfer by grid-generated turbulence in the presence of a mean scalar gradient, J. Fluid Mech. **764**, 52 (2014).

[44] Y. Ito, T. Watanabe, K. Nagata, and Y. Sakai, Turbulent mixing of a passive scalar in grid turbulence, Phys. Scr. **91**, 074002 (2016).

[45] T. Watanabe, Y. Sakai, K. Nagata, Y. Ito, and T. Hayase, Implicit large eddy simulation of a scalar mixing layer in fractal grid turbulence, Phys. Scr. **91**, 074007 (2016).

[46] S. Corrsin, Remarks on turbulent heat transfer: An account of some features of the phenomenon in fully turbulent regions, in *Proc. 1st Iowa Symp. on Thermodynamics* (Johns Hopkins University, Baltimore, 1953), pp. 5–30.

[47] S. Balay, S. Abhyankar, M. Adams, J. Brown, P. Brune, K. Buschelman, V. Eijkhout, W. Gropp, D. Kaushik, and M. Knepley, PETSc users manual revision 3.5, Technical report, Argonne National Laboratory (2014).

[48] I. Paul, Evolution of velocity and scalar gradients in a spatially developing turbulence, Ph.D. thesis, Imperial College, London (2017).

[49] I. Paul, G. Papadakis, and J. C. Vassilicos, DNS of heat transfer from a cylinder immersed in the production and decay regions of grid-element (unpublished).

[50] I. Paul, G. Papadakis, and J. C. Vassilicos, On the skewness of passive scalar gradients in heated grid-element turbulence (unpublished).

[51] A. Tsinober, *An Informal Conceptual Introduction to Turbulence*, Vol. 483 (Springer, Berlin, 2009).

[52] H. Tennekes and J. L. Lumley, *A First Course in Turbulence* (MIT Press, Cambridge, MA, 1972).

[53] M. Lesieur, *Turbulence in Fluids*, Vol. 40 (Springer Science & Business Media, New York, 2012).

[54] M. Lesieur, C. Montmory, and J. P. Chollet, The decay of kinetic energy and temperature variance in three-dimensional isotropic turbulence, Phys. Fluids **30**, 1278 (1987).

[55] B. E. Launder, On the computation of convective heat transfer in complex turbulent flows, J. Heat Transfer **110**, 1112 (1988).

[56] A. N. Kolmogorov, The local structure of turbulence in incompressible viscous fluid for very large Reynolds numbers, Dokl. Akad. Nauk SSSR **30**, 299 (1941).

[57] S. K. Lee, A. Benaissa, L. Djenidi, P. Lavoie, and R. A. Antonia, Scaling range of velocity and passive scalar spectra in grid turbulence, Phys. Fluids **24**, 075101 (2012).

[58] G. R. Ruetsch and M. R. Maxey, Small-scale features of vorticity and passive scalar fields in homogeneous isotropic turbulence, Phys. Fluids **3**, 1587 (1991).

[59] G. R. Ruetsch and M. R. Maxey, The evolution of small-scale structures in homogeneous isotropic turbulence, Phys. Fluids **4**, 2747 (1992).

[60] G. Brethouwer, J. C. R. Hunt, and F. T. M. Nieuwstadt, Micro-structure and Lagrangian statistics of the scalar field with a mean gradient in isotropic turbulence, J. Fluid Mech. **474**, 193 (2003).

[61] R. Betchov, Numerical simulation of isotropic turbulence, Phys. Fluids **18**, 1230 (1975).

[62] B. Ganapathisubramani, K. Lakshminarasimhan, and N. T. Clemens, Investigation of three-dimensional structure of fine scales in a turbulent jet by using cinematographic stereoscopic particle image velocimetry, J. Fluid Mech. **598**, 141 (2008).

[63] G. Gulitski, M. Kholmyansky, W. Kinzelbach, B. Lüthi, A. Tsinober, and S. Yorish, Velocity and temperature derivatives in high-Reynolds-number turbulent flows in the atmospheric surface layer. Part 1. Facilities, methods and some general results, J. Fluid Mech. **589**, 57 (2007).

[64] K. Ohkitani, Numerical study of comparison of vorticity and passive vectors in turbulence and inviscid flows, Phys. Rev. E **65**, 046304 (2002).